PAPER

Check for updates

Hierarchically porous N-doped carbon nanosheets with atomically dispersed Fe/Co dual-metallic sites for efficient and robust oxygen electrocatalysis in Zn–air batteries†

Zheng-Qi Liu,[a] Fei-Xiang Ma, ID *[a] Yu-Xuan Xiong,[a] Meng-Tian Zhang,[a] Yue Du,[ab]
Liang Zhen[acd] and Cheng-Yan Xu ID *[ac]

The design and synthesis of non-precious-metal single-atom catalysts with favorable coordination environments and abundant accessible active sites to boost the sluggish oxygen reduction reaction (ORR) is highly desirable for both fuel cells and metal–air batteries. In this work, atomic Fe/Co dual sites anchored on N-doped carbon nanosheets (Fe/Co–N–C NSs) with thickness below 8 nm are fabricated via a polyvinylpyrrolidone-directed chemical blowing strategy together with a subsequent pickling step and metal atom trapping. Detailed characterizations including atomic-resolved HAADF-STEM observation and BET analysis revealed that the dual-metallic Co/Fe–N_x moieties are uniformly dispersed in highly porous Fe/Co–N–C NSs with abundant hierarchical pores below 4 nm. Thanks to the synergic effect of dual-metallic Fe/Co–N_x active sites and abundant accessible catalytic sites provided from the hierarchically porous nanosheet structures, the resultant Fe/Co–N–C NSs delivered excellent ORR performance in 0.1 M KOH with a positive half-wave potential ($E_{1/2}$) of 0.88 V vs. RHE, high kinetic current density (J_k) of 24.8 mA cm^{-2} at 0.85 V and robust stability, exceeding those of commercial Pt/C and mono-metallic Fe–N–C NSs. When Fe/Co–N–C NSs were employed as air cathode catalysts for primary Zn–air batteries, the assembled cells delivered an open-circuit voltage up to 1.52 V and a peak power density of 165 mW cm^{-2}.

Introduction

High-performance electrocatalysts for the oxygen reduction reaction (ORR) are highly demanded for advanced electrochemical energy storage and conversion devices including metal–air batteries and fuel cells.[1–6] Platinum-group metals (PGMs) are widely recognized as efficient ORR catalysts because of their unique electronic structures. However, the concerns related to scarcity, high cost and unsatisfactory stabilities of PGM catalysts preclude their large-scale commercialization.[7–11] In this regard, transition metal and nitrogen co-doped carbon catalysts (TM–N–C, where TM represents Fe, Co, Mn, Cu, etc.), especially Fe–N–C, are the most promising alternative to PGM catalysts by

virtue of their low cost, high activity and robust stability.[5,12–17] Among the Fe–N–C catalysts, single Fe atoms coordinated with nitrogen (Fe–N_x) moieties are commonly identified as the real catalytic sites for absorbing O_2 and accelerating the subsequent ORR kinetics.[18–21] To further boost the ORR activities of Fe–N–C catalysts, several strategies have been developed, including increasing the exposed Fe–N_x active sites, modulating the local coordination environments of the central metal atoms, and incorporating another active metal atom to generate bimetal–N–C species.[14,22–26] Among them, the unique bimetal–N–C species can not only offer more favorable M–N_x active sites but also create fantastic synergistic effects to break the bond in O_2 during the ORR, significantly boosting the electrocatalytic activities.[27–30] More importantly, theoretical calculations also reveal the synergistically enhanced ORR activity of bimetal–N–C active sites partially through weakening the O–O bonds and promoting the reduction of O_2 to OOH*.[31] Therefore, encapsulating heterometal atoms into an Fe–N–C matrix to form unique bimetal–N–C is supposed to greatly enhance the ORR activities.[32–35]

The morphologies and porous configurations of Fe–N–C catalysts are also critical to acquire excellent ORR activities through generating more accessible active sites, faster electron

a Sauvage Laboratory for Smart Materials, School of Materials Science and Engineering, Harbin Institute of Technology (Shenzhen), Shenzhen 518055, China. E-mail: mafeixiang@hit.edu.cn, cy_xu@hit.edu.cn

b Peng Cheng Laboratory, Shenzhen 518055, China

c MOE Key Laboratory of Micro-Systems and Micro-Structures Manufacturing, Harbin Institute of Technology, Harbin 150080, China

d School of Materials Science and Engineering, Harbin Institute of Technology, Harbin 150001, China

and mass transportation pathways and higher surface areas.[36–38] Among the diverse carbon structures to support the isolated Fe atoms, 2D carbon nanosheets have attracted intense attention because of their favorable structural advantages, including high electronic conductivity for rapid electron transport and high exposed surface areas for catalytic reactions.[39,40] In particular, carbon nanosheets can easily interconnect with each other to form a 3D conductive network structure, further improving the electron/ion transfer efficiency.[41–43] Moreover, designing hierarchical pore structures in 2D carbon nanostructures can simultaneously take mass transfer and the active sites into account, as mesopores benefit the fluent mass transportation and micropores are conducive to generating more active sites for catalytic reactions. Therefore, developing an efficient approach to prepare hierarchically porous 2D Fe–N–C catalysts for the ORR is highly desirable.

In this work, dual-metallic FeCo atomic sites encapsulated in N-doped porous carbon nanosheets (Fe/Co–N–C NSs) are fabricated through rationally pyrolyzing the chelating mixture of iron nitrate and PVP together with atomic trapping of transition-metal ions. Hierarchical porous nanosheets with abundant pores (1–5 nm) were created by the selected etching of Fe-containing nanocrystals embedded in the intermediate carbon nanosheets, produced by a unique chemical blowing process. Benefitting from the highly porous nanosheet structure and dense Fe/Co–N_x active sites exposed to the electrolyte, the dual-metallic Fe/Co–N–C NSs could be used as high-performance ORR electrocatalysts. In prticular, the Fe/Co–N–C NSs delivered better ORR activity compared to carbon nanosheets with single Fe atoms only (Fe–N–C), suggesting a synergistic enhancement of the ORR performance in the dual-metallic Fe/Co–N_x active sites. Finally, the Fe/Co–N–C NSs were also investigated as high-performance air-cathode catalysts for primary Zn–air batteries (ZABs).

Experimental

Materials fabrication

All the chemicals were used without further purification. In a typical synthesis, 1 g of polyvinylpyrrolidone (PVP, K30) and 1 g of Fe(NO$_3$)$_3$·9H$_2$O were first dissolved into 15 mL of deionized water. Then, the solution was continuously stirred and sonicated at room temperature to obtain a sticky yet homogeneous solution. The solution was dried at 80 °C in an oven and the fine powder with orange color was obtained after grinding. The as-obtained powder was annealed at 200 °C and maintained for 0.5 h in a tube furnace. Then, the furnace temperature was further raised to 500 °C for 2 h with a ramping rate of 3 °C min^{-1}. After that, the as-achieved fluffy powder was immersed in 2 M HCl solution to remove most iron-containing compounds, generating highly porous carbon nanosheets implanted with trace amounts of iron atoms. Subsequently, the resulting carbon powder (100 mg) and Co(NO$_3$)$_2$·6H$_2$O (9.0 μmol) were further dispersed in 40 mL of deionized water and stirred for 2 h to guarantee that the Co^{2+} ions can be

fully adsorbed on the surface of the carbon nanosheets. After the adsorption, the relevant carbon powder and 1 g of dicyandiamide were subjected to a secondary calcination (900 °C for 2 h) in a tube furnace to obtain the targeted Fe/Co–N–C NSs. As a comparison, the same molar amounts of Ni^{2+}, Mn^{2+}, Cu^{2+}, and Fe^{3+} ions were adsorbed on the carbon nanosheets, which were labeled as Fe/Mn–N–C, Fe/Cu–N–C, Fe/Ni–N–C, and Fe/Fe–N–C. Moreover, Fe/Co–N–C NSs were also calcined at different temperatures to explore the influence of calcination temperature on the catalytic properties. As a control experiment, Fe–N–C is synthesized via the same process except that no additional transition-metal salts were adsorbed.

Material characterizations

Powder X-ray diffraction (XRD) patterns were profiled on an X-ray diffractometer (PANalytical). Scanning electron microscope (SEM) images were recorded on a SUPRA™ 55 (ZEISS, Germany) microscope. The thickness of the carbon nanosheets was analyzed by an AFM (Bruker DIMENSION icon). A transmission electron microscope (TEM; JEOL JEM-3200FS) equipped with energy dispersive X-ray spectroscopy (EDX) was employed to observe the microstructure and element dispersion of C, N, Fe and Co in the catalyst. Raman spectra were profiled on a Renishaw confocal microscope (532 nm laser). Brunauer–Emmett–Teller (BET) and the pore structure were characterized by nitrogen adsorption–desorption measurements with a Micromeritics/ASAP 2460 instrument, and the pore distribution was investigated by the density functional theory (DFT) method. Elemental analyses were conducted on a Thermo Scientific ESCALAB 250Xi X-ray photoelectron spectroscopy (XPS) spectrometer and an inductively coupled plasma-optical emission spectrometry (ICP-OES) system.

Electrochemical measurements

The Fe/Co–N–C and other comparative samples were prepared by mixing 7 mg of the catalyst in 500 μL of solution containing 230 μL of ethanol, 230 μL of isopropanol and 40 μL of 5% Nafion solution, followed by ultrasonication for 30 min to form homogeneous catalyst inks. In comparison, a commercial 20% wt Pt/C sample was tested under identical conditions by dispersing 2 mg of the catalyst in 500 μL of solution. A certain volume of the catalyst ink was dropped onto a well-polished glassy carbon rotating disk electrode (RDE) or rotating ring disk electrode (RRDE). The loading mass of nonprecious catalyst and Pt/C was 0.6 mg cm^{-2} and 0.2 mg cm^{-2}, respectively. The detailed testing conditions can be found in the ESI.†

Zn–air battery performance

Zn–air batteries (ZABs) were assembled by coating the catalyst on hydrophobic carbon cloth with a loading mass of 1 mg cm^{-1} as the air cathode. A polished Zn plate was employed as an anode and the void between the two electrodes was filled with 6 M KOH solution with 0.2 M Zn(OAC)$_2$ as additive. The open-circuit voltage and discharge polarization curve of the battery were measured on an electrochemical workstation (CHI 760E).

The galvanostatic test was performed using a battery test system (Land 3001A) at room temperature.

Results and discussion

Physical characterizations

The fabrication process of Fe/Co–N–C NSs is schematically illustrated in Fig. 1. First, the mixed solution of PVP and iron nitrate was dried thoroughly at 80 °C and subsequently calcined at 500 °C in inert gas flow. When the calcination temperature is above the glass transition temperature ($\sim$200 °C), the molten fluid of PVP would be blown up to form a bubble-like structure by abundant gas released from the fast decomposition of iron nitrate. Meanwhile, the Fe-contained nanoparticles with a size of several nanometers are formed and uniformly decorated into carbon nanosheets by *in situ* carbothermal reduction of iron nitrate at 500 °C (Fig. S1 and S2, ESI†). SEM images in Fig. S1a and b (ESI†) show that the nanosheets were connected together to form a 3D sponge-like structure. TEM images in Fig. S1c–e (ESI†) demonstrated that tiny nanoparticles with a size of several nanometers are densely embedded in the carbon nanosheets. The HRTEM image revealed that the Fe-containing nanoparticles are well-crystallized with clear lattice fringes (Fig. S1f, ESI†). The XRD pattern in Fig. S2 (ESI†) suggested that the Fe-containing nanoparticles are mixtures of Fe, Fe_3O_4 and Fe_3C. The EDS mapping images (Fig. S1g, ESI†) revealed that C, N, O and Fe atoms are uniformly distributed in the whole nanosheets, indicating that the Fe-containing nanoparticles were homogeneously embedded in the N-doped carbon nanosheet matrix. After that, the Fe-containing nanoparticles embedded in the carbon nanosheets can be removed by strong acid washing, leading to the generation of highly porous carbon nanosheets. Notably, a certain amount of atomic iron species remained in the carbon nanosheets, and after adsorption of Co^{2+} ions in dilute cobalt nitrate solution and subsequent high-temperature treatment in a CN-rich atmosphere produced by dicyandiamide decomposition, dual-metallic Fe/Co–N–C NSs would be generated through nitrogen trapping and bonding Fe and Co atoms in the N-doped carbon matrix.

The morphology of the Fe/Co–N–C NSs was investigated by SEM and TEM. As shown in Fig. 2a, the Fe/Co–N–C NSs were very fluffy and exhibited a distinct porous lamellar structure due to the chemical blowing of PVP with the assistance of iron nitrate. From the high-magnification SEM image (Fig. 2b), the carbon nanosheets are connected together to form a sponge-like shape. Note that after breaking the sponge-like product through long-term ultrasonic treatment, well-dispersed carbon nanosheets would be generated. The AFM image in Fig. 2c confirmed that the thickness of the Fe/Co–N–C NSs is less than 8 nm, which was not reported so far in the PVP derived carbon nanosheets *via* the chemical blowing strategy.[40,44] The low-magnification TEM image in Fig. 2d shows a large piece of carbon nanosheet with an even contrast, indicating that the thickness of the Fe/Co–N–C NSs was uniform. The selected-area electron diffraction (SAED) pattern of Fe/Co–N–C (inset in
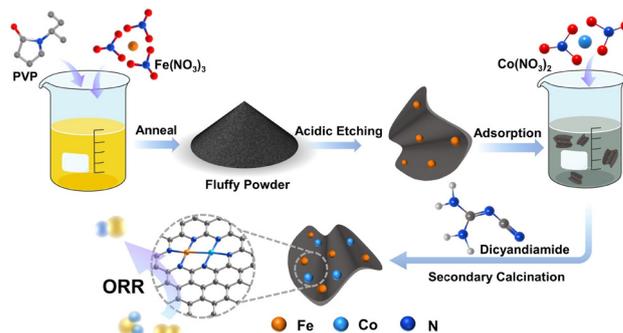

Fig. 1 Schematic procedure for the synthesis of the Fe/Co–N–C electrocatalyst.

Fig. 2d) displays two distinct diffraction rings, which were associated with the (100) and (002) crystallographic planes of the graphitic carbon.[45] The high magnification TEM and high-angle annular dark-field scanning transmission electron microscope (HAADF-STEM) images clearly reveal that a large number of pores are uniformly distributed in the carbon matrixes (Fig. 2e and Fig. S3, ESI†). Furthermore, the high-resolution TEM (HRTEM) image (Fig. 2f) of Fe/Co–N–C NSs shows that the carbon nanosheets were partially graphitic with a lattice distance of 0.36 nm, larger than the value of graphite (0.34 nm). This high lattice distance could be partially attributed to the high distortion of carbon nanostructures by the heteroatom substitutions (Fe, Co and N) and the low graphitization. Due to the Z-contrast of metal and nitrogen/carbon atoms, the atomic-resolved HAADF-STEM images of Fe/Co–N–C (Fig. 2g) showed that many small single dots were well distributed in the carbon support, indicating that most metal (Fe or Co) atoms were isolated from each other. Impressively, there were also considerable bright dual dots (marked with yellow circles) distributed in the carbon framework, suggesting the formation of dual-metal (Fe–Co, Fe–Fe and Co–Co) dimers. These well-dispersed Fe/Co single-atoms are supposed to be effective active sites for the ORR, ensuring superior catalytic capacity. The actual loading mass of Fe and Co in the Fe/Co–N–C NSs was confirmed to be 2.0 wt% and 0.1 wt%, respectively, determined by ICP-OES. The corresponding element mapping diagram (Fig. 2h) demonstrated the homogeneous distribution of C, N, Fe and Co elements, further confirming that iron and cobalt atoms are homogeneously immobilized in the carbon nanosheets.

XRD analysis was used to determine the crystal structure of the as-prepared samples. As shown in Fig. 3a, the XRD patterns of both Fe/Co–N–C and Fe–N–C have two broad peaks centered at $\sim$24.0° and $\sim$43.5° belonging to the (002) and (100) planes of graphite, respectively, suggesting an amorphous nature of carbon.[46] The interplanar spacing of the (002) planes was calculated to be about 0.37 nm according to the Bragg equation, close to the HRTEM result. No diffraction peaks belonging to crystalline metals or metal compounds can be detected. Notably, the intensity and full width at half maximum (FWHM) of the (002) plane in Fe/Co–N–C were obviously lower than that of
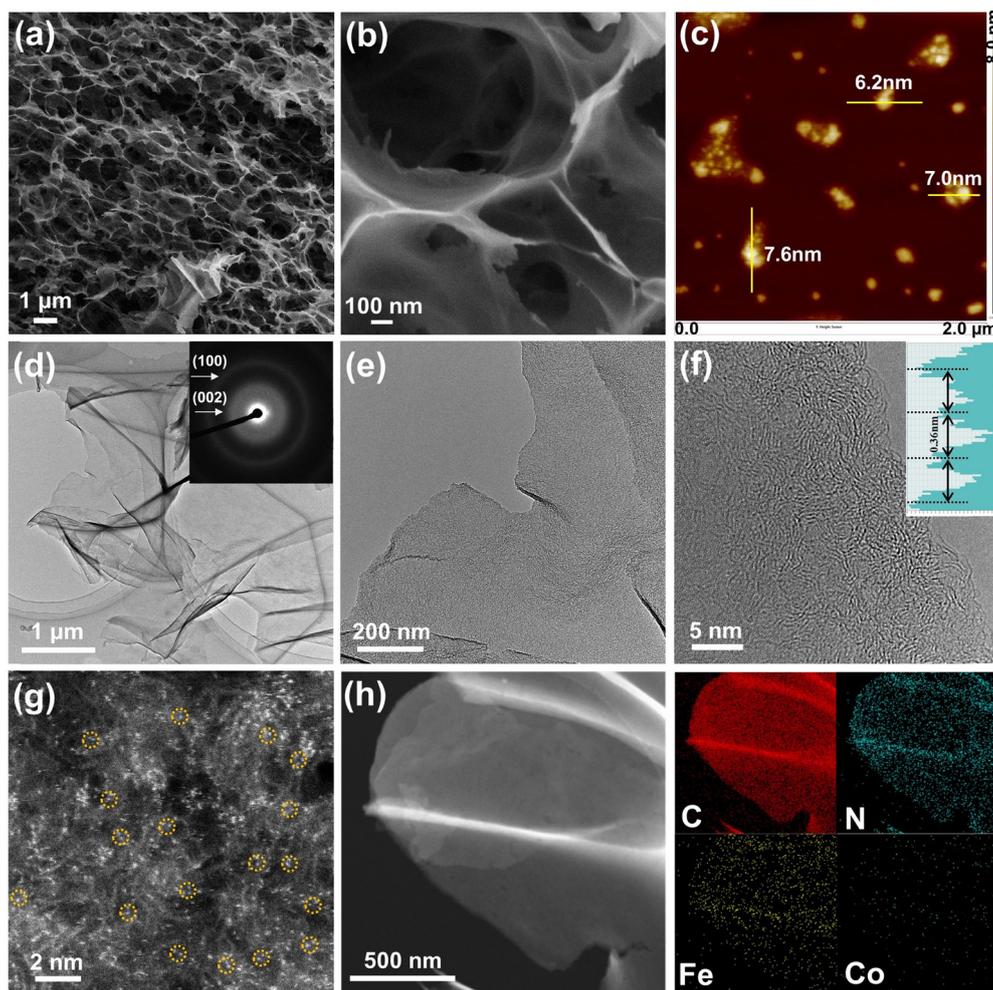
Fig. 2 Microstructure characterization of the as-prepared Fe/Co–N–C NSs. (a and b) SEM, (c) AFM, (d and e) TEM, and (f) HRTEM images (inset in (d) is the corresponding SAED pattern and inset in (e) is the contrast intensity profile of the lattice fringes), (g) atomic-resolved HADDF-STEM image of Fe/Co–N–C, and the dual-metal dimers (Fe–Co, Fe–Fe and Co–Co) are labelled with yellow circles, and (h) elemental mapping of C, N, Fe and Co of Fe/Co–N–C.

Fe–N–C, indicating that extra introduction of Co atoms might disorder the crystal lattice and decrease the crystallinity of carbon nanosheets. Two distinct peaks in the Raman spectra (Fig. 3b) located at 1350 cm^{-1} and 1580 cm^{-1} correspond to the defect-related D bands and sp^2-hybridized carbon-correlated G bands, respectively.[47] The slightly higher I_D/I_G ($\sim$1.73) of Fe/Co–N–C than that of Fe–N–C ($\sim$1.71) reveals low crystallinity and rich defects in the Fe/Co–N–C NSs, consistent with the XRD results. The pore structure characteristics of the Fe/Co–N–C NSs were analyzed by N$_2$ adsorption–desorption isotherms (Fig. 3c). Fe/Co–N–C displayed a typical type-I isothermal curve, indicating that Fe/Co–N–C NSs contained rich micropores. The pore-size distributions (inset in Fig. 3c) clearly proved the presence of abundant micropores and mesopores with size distribution of below 4 nm in the Fe/Co–N–C NSs, in line with the TEM observations. The rich micropores and mesopores as well as the thin carbon nanosheets in the Fe/Co–N–C NSs contributed to a high specific surface area of 1095.6 m^2 g^{-1}. Considering the thin nanosheet matrix below 8 nm, the mesopores in the

Fe/Co–N–C NSs benefit the fluent mass transportation, while the micropores are conducive to generating more active sites for catalytic reactions. Therefore, such highly porous structures would endow Fe/Co–N–C NSs with dense accessible active sites and extraordinary electron transfer efficiency.[48–51] XPS was performed to investigate the compositions and chemical states of Fe/Co–N–C and Fe–N–C NSs. The full-scan XPS spectra proved the presence of N, C and O elements (Fig. 3d). The high-resolution Fe 2p spectrum (Fig. S4, ESI†) has two strong peaks located at 710.8 eV and 723.9 eV, belong to the binding energies of the 2p$_{3/2}$ and 2p$_{1/2}$ orbitals of Fe^{2+}. And the two peaks in the high-resolution Co 2p spectrum (Fig. S5, ESI†) can be assigned to Co^{2+} 2p$_{3/2}$ and Co^{2+} 2p$_{1/2}$. Such results indicate that the valence of both Co and Fe is 2+. The high-resolution C 1s spectrum (Fig. 3e) of the Fe/Co–N–C NSs could be deconvoluted into three peaks, corresponding to the characteristic peaks of C–C (284.8 eV), C–N (285.8 eV) and C=O (289.0 eV). The N content is as high as $\sim$6% in both Fe/Co–N–C and Fe–N–C based on the XPS results. The N 1s spectra (Fig. 3f) can be
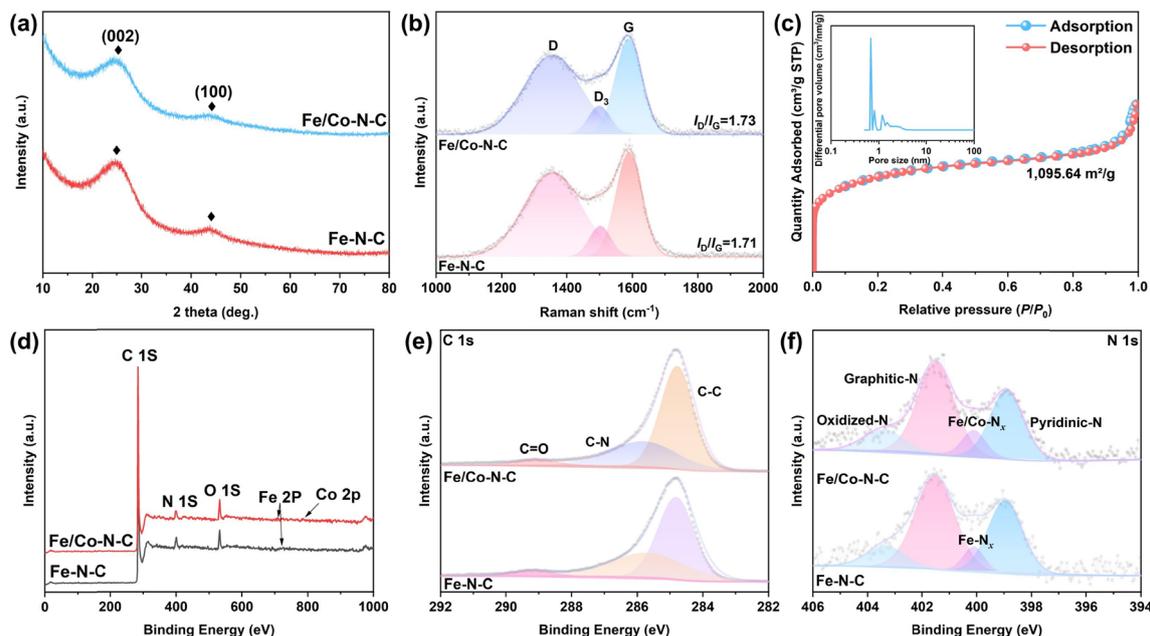
Fig. 3 (a) XRD patterns and (b) Raman spectra of Fe–N–C and Fe/Co–N–C, (c) nitrogen adsorption–desorption isotherm and pore size distribution curve (inset in (c)) of Fe/Co–N–C, (d) XPS survey spectra, (e) high-resolution C 1s and (f) high-resolution N 1s spectra of Fe–N–C and Fe/Co–N–C; the inset in (f) is the corresponding content of different N species.

deconvoluted into pyridinic N (398.9 eV), Fe/Co–N (400.1 eV), graphite N (401.5 eV) and oxidized N. The high fraction of pyridinic ($\sim$45%) and graphic N ($\sim$43%) in the Fe/Co–N–C NSs is proposed to be responsible for the active sites for the ORRs.[52,53] In addition, the decomposition of dicyandiamide would generate a large number of unliganded N sites, which can also stabilize the highly active Fe and Co atoms through generating Fe/Co–N_x moieties during the annealing process.[54]

Electrochemical performance

Fe/Co–N–C NSs were expected to exhibit excellent ORR catalytic activity due to the structural and compositional merits. The electrocatalytic properties of catalysts including Fe/Co–N–C NSs were investigated using a three-electrode system in alkaline media. To optimize the annealing temperature, the ORR activities of the samples obtained at different temperatures (800, 900 and 1000 °C) were first evaluated (Fig. S4, ESI†). Compared to the catalysts obtained at 800 and 1000 °C, the Fe/Co–N–C NSs obtained at 900 °C exhibited the best catalytic activity (detailed discussion was inserted in ESI†). In addition, we also optimized the metal loading in Fe/Co–N–C to achieve the best catalytic activity (Fig. S7, ESI†), which showed that the optimal Co content is 0.1 wt%. Therefore, all the following tests were based on the samples obtained at 900 °C. As shown in Fig. 4a, the Fe/Co–N–C NSs delivered better activity than commercial Pt/C and mono-metallic Fe–N–C determined by the linear scanning voltammetry (LSV) curves.

The Fe/Co–N–C NSs exhibited more positive onset potential (E_{onset} = 1.0 V vs. RHE) and half-wave potential ($E_{1/2}$ = 0.88 V vs. RHE), and higher ultimate current density (J_L = 6.2 mA cm^{-2}), than commercial Pt/C ($E_{1/2}$ = 0.84 V, E_{onset} = 0.99 V,

J_L = 5.1 mA cm^{-2}) and Fe–N–C ($E_{1/2}$ = 0.86 V, E_{onset} = 0.97 V, J_L = 5.3 mA cm^{-2}). The mass activity of the Fe/Co–N–C NSs is significantly higher than that of Fe–N–C and Pt/C (Fig. S8, ESI†), suggesting the high metal utilization. The remarkable ORR kinetics of the Fe/Co–N–C NSs was confirmed by the smaller Tafel slope (62 mV dec^{-1}) than that of commercial 20% Pt/C (80 mV dec^{-1}) and the Fe–N–C (76 mV dec^{-1}) (Fig. 4b). The superior ORR kinetics for the Fe/Co–N–C NSs could be partially ascribed to the possible synergistic interaction of FeCo–N_x dual sites and the nitrogen species, which could narrow the cleavage barrier of O–O bonds to achieve high ORR activity.[34] Importantly, the kinetic current density (J_K) representing the electrochemical intrinsic activity was 24.8 mA cm^{-2} for Fe/Co–N–C at 0.85 V, which is significantly higher than that of Fe–N–C (7.2 mA cm^{-2}) and Pt/C (3.6 mA cm^{-2}). The turnover frequency (TOF) of the Fe/Co–N–C catalyst and the control samples was calculated based on the kinetic currents and the metal contents from ICP-OES results, assuming that all the Fe and Co atoms are atomically dispersed and coordinated with nitrogen species. As shown in Fig. 4c, the Fe/Co–N–C ($\sim$0.058 e$^-$ site^{-1} s^{-1}) showed a higher TOF than Fe–N–C ($\sim$0.039 e$^-$ site^{-1} s^{-1}) at 0.8 V vs. RHE. Compared to mono-metallic Fe–N–C, the excellent intrinsic activity of dual-metallic Fe/Co–N–C can be ascribed to the synergistic effect of atomic Fe/Co–N_x dual sites in Fe/Co–N–C through effectively modulating the electronic structure.

Based on the polarization curves of Fe/Co–N–C at different rotation rates (Fig. 4d), the average electron transfer number (n) according to the K–L equation (inset in Fig. 4d) was calculated to be $\approx$4, revealing high-efficiency reduction of O_2 to H_2O. To reveal the electro-transfer mechanism, RRDE tests were carried
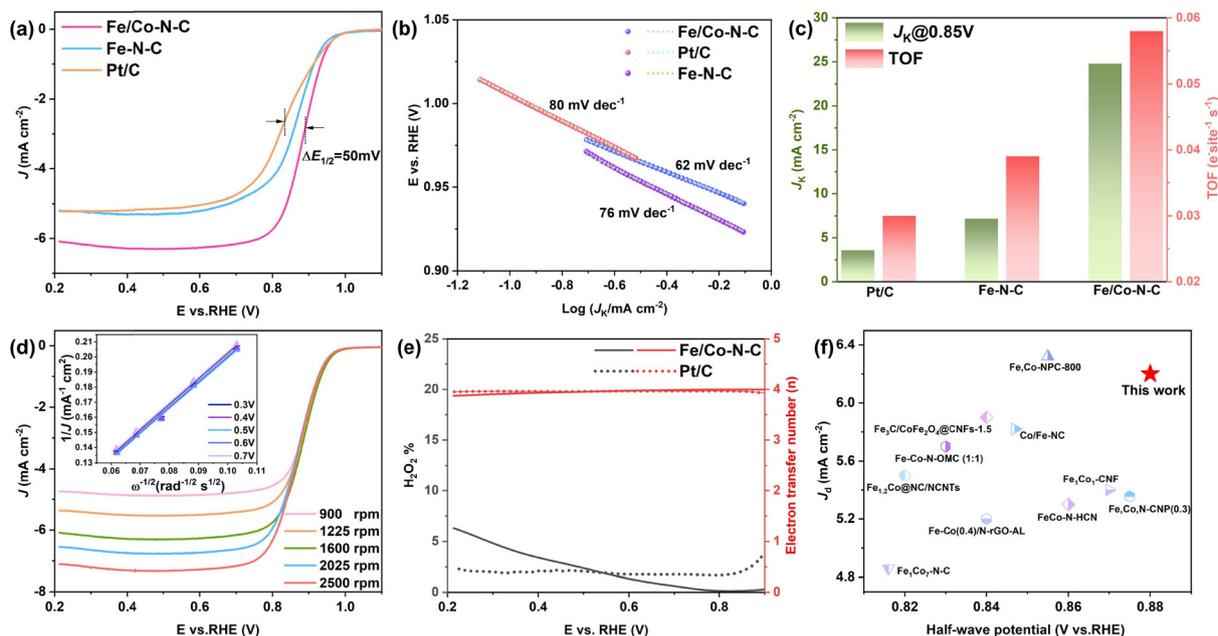
Fig. 4 (a) LSV curves (sweep rate: 5 mV s^{-1}), (b) corresponding Tafel plots, (c) the histogram of J_K and TOF at 0.85 V vs. RHE, (d) LSV curves of Fe/Co–N–C at various rotating rates in 0.1 M KOH solution and the corresponding K–L fitting lines at various potentials, (e) the electron transfer number (n, top) and the H$_2$O$_2$ yield (bottom) of Fe/Co–N–C and Pt/C, and (f) comparison of Fe/Co–N–C with other reported Fe/Co–N–C electrocatalysts in alkaline solution.

out for both Fe/Co–N–C and Pt/C (Fig. 4e). From 0.2 V to 0.9 V, the number of transferred electrons of Fe/Co–N–C was between 3.88 and 3.99, and the peroxide yield was almost kept below 5%, very close to that of Pt/C. Thus, the ORR of Fe/Co–N–C NSs followed a typical four-electron pathway. Finally, the stabilities and methanol tolerance of the relevant catalysts were also investigated. After 12 h chronoamperometry tests, the current decay of Fe/Co–N–C was only 7.3%, while that of Pt/C was 18.1%, illustrating the remarkable stability of the Fe/Co–N–C catalyst (Fig. S9, ESI†). In addition, the methanol tolerance of the Fe/Co–N–C and Pt/C catalysts was evaluated. Notably, the current change was negligible for Fe/Co–N–C after introducing 1 M methanol, whereas a dramatic current loss occurs for Pt/C under the same conditions (Fig. S10, ESI†). These results clearly indicated that the dual-metallic Fe/Co–N–C possessed excellent tolerance against methanol poisoning, indicating its potential application in fuel cells. In order to investigate the influence of the secondary transition-metal ion on the ORR activity of dual-metallic Fe/M–N–C NSs, Fe/Mn–N–C, Fe/Cu–N–C, Fe/Ni–N–C and Fe/Fe–N–C catalysts were also fabricated by adsorbing Mn^{2+}, Cu^{2+}, Ni^{2+} and Fe^{3+} ions, respectively, with the same atomic proportions and fabrication process (Fig. S11, ESI†). By comparing their ORR performance, we found that all the dual-metallic catalysts exhibited superior activity over commercial Pt/C, and the Fe/Co–N–C catalyst delivered the best ORR activity compared to other dual-metallic catalysts. All in all, the ORR activity of dual-metallic Fe/Co–N–C NSs is comparable to that of various bimetal–N–C catalysts previously reported (Fig. 4f and Table S1, ESI†).

Taking all of the above results together, the Fe/Co–N–C NSs exhibit excellent ORR activity as well as remarkable durability in alkaline media, which can be reasonably ascribed to the following prominent advantages: (1) the unique thin nanosheets with abundant hierarchical pores can provide a large number of electron/electrolyte channels and increase the amount of exposed active sites; (2) abundant highly-dispersed metal–N$_x$ species can be employed as highly active ORR sites with good structural stability; (3) the synergistic effect of atomic Fe/Co–N$_x$ dual sites could boost the ORR activity via modulating the electronic and geometric structures, which would reduce the energy barriers of the rate-limiting process of the ORR. Therefore, these unique composition and structure merits endow Fe/Co–N–C NSs with outstanding ORR performance, surpassing that of mono-metallic Fe–N–C and benchmark Pt/C catalysts.

Inspired by the impressive ORR performance, practical ZABs were assembled and investigated using Fe/Co–N–C NSs as air cathode catalysts. The Fe/Co–N–C catalyst is supported on hydrophobic carbon cloth to construct an air-breathable electrode and commercial Pt/C with the same loading mass was also used as a comparison sample (Fig. 5a). The open circuit voltage of the Fe/Co–N–C electrode (Fig. 5b) is high as ~1.52 V, which is much higher than that of commercial Pt/C (~1.40 V). As shown in Fig. 5c, the primary ZAB exhibited a maximum power density of 165 mW cm^{-2}, significantly surpassing that of Pt/C (121 mW cm^{-2}), well matching the superb ORR activity of Fe/Co–N–C NSs. Note that the peak power density based on the Fe/Co–N–C air-cathode is comparable and even better than most reported ZABs based on efficient ORR catalysts. Impressively, a stable voltage output of ~1.27 V can be maintained for more than 50 hours without obvious decline at a constant discharge current density of 5 mA cm^{-2}, demonstrating the
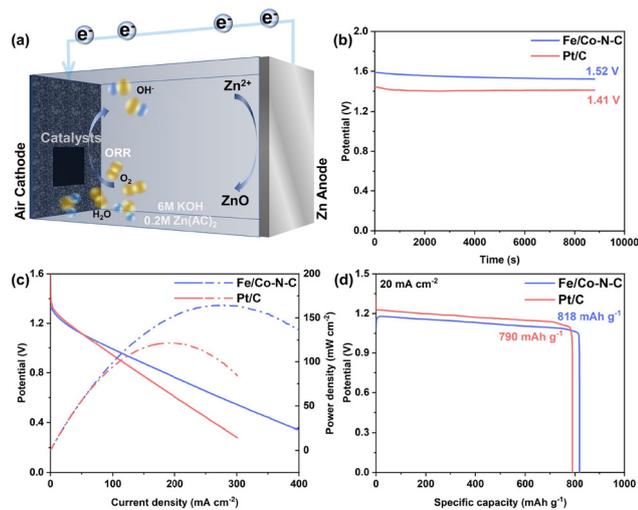
Fig. 5 (a) Schematic representation of a Zn–air battery, (b) open circuit plots of the Zn–air battery using Fe/Co–N–C and Pt/C as air electrodes, (c) discharge polarization curves and corresponding power density curves using Fe/Co–N–C and commercial Pt/C (20 wt%) as the air cathode, respectively, and (d) specific discharging capacities of the cell with Fe/Co–N–C and Pt/C air cathodes at 20 mA cm^{-2}, respectively.

robust durability of Fe/Co–N–C based air electrodes (Fig. S12, ESI†). In addition, when the current density is 20 mA cm^{-2}, Fe/Co–N–C enabled the assembled ZAB to exhibit a high specific capacity of 818 mA h g$_{Zn}^{-1}$, which outperforms that of Pt/C with 790 mA h g$_{Zn}^{-1}$ (Fig. 5d). The above encouraging results revealed that Fe/Co–N–C NSs hold great potential in the practical application of ZABs.

Conclusions

In summary, a unique chemical blowing strategy together with a pickling step and subsequent atomic trapping was proposed to prepare dual-metallic Fe/Co–N–C NSs with abundant hierarchical pores. Thanks to the abundant exposed Fe/Co–N$_x$ active sites, and the synergistic effect of atomic Fe/Co–N$_x$ dual sites and hierarchical porous structures with high surface area, the Fe/Co–N–C NSs exhibited better ORR performance than mono-metallic Fe–N–C and commercial Pt/C. When using Fe/Co–N–C NSs as air cathode electrocatalysts for ZABs, the assembled cells delivered a high OCV of 1.52 V and a remarkable power peak density of 165 mW cm^{-2}. Our research highlights the importance of engineering the microstructures of carbon supporting and modulating the coordination environment of M–N–C catalysts.

Conflicts of interest

There are no conflicts to declare.

Acknowledgements

Notes and references

1 R. F. Service, *Science*, 2002, **296**, 1222–1224.
2 M. K. Debe, *Nature*, 2012, **486**, 43–51.
3 L. Du, V. Prabhakaran, X. Xie, S. Park, Y. Wang and Y. Shao, *Adv. Mater.*, 2021, **33**, e1908232.
4 S. J. Peng, X. P. Han, L. L. Li, S. L. Chou, D. X. Ji, H. J. Huang, Y. H. Du, J. Liu and S. Ramakrishna, *Adv. Energy Mater.*, 2018, **8**, 1800612.
5 L. M. Deng, F. Hu, M. Y. Ma, S. C. Huang, Y. X. Xiong, H. Y. Chen, L. L. Li and S. J. Peng, *Angew. Chem., Int. Ed.*, 2021, **60**, 22276–22282.
6 Z. X. Pei, L. Y. Ding, C. Wang, Q. Q. Meng, Z. W. Yuan, Z. Zhou, S. L. Zhao and Y. Chen, *Energy Environ. Sci.*, 2021, **14**, 4926–4935.
7 X. Liu and L. M. Dai, *Nat. Rev. Mater.*, 2016, **1**, 16064.
8 L. Z. Bu, S. J. Guo, X. Zhang, X. Shen, D. Su, G. Lu, X. Zhu, J. L. Yao, J. Guo and X. Q. Huang, *Nat. Commun.*, 2016, **7**, 11850.
9 L. L. Li, D. S. Yu, P. Li, H. J. Huang, D. Y. Xie, C. C. Lin, F. Hu, H. Y. Chen and S. J. Peng, *Energy Environ. Sci.*, 2021, **14**, 6419–6427.
10 Z. S. Ye, P. Li, W. T. Wei, C. Huang, L. W. Mi, J. L. Zhang and J. J. Zhang, *Adv. Sci.*, 2022, **9**, 2200067.
11 Z. Zhou, Y. Kong, H. Tan, Q. W. Huang, C. Wang, Z. X. Pei, H. Z. Wang, Y. Y. Liu, Y. H. Wang, S. Li, X. Z. Liao, W. S. Yan and S. L. Zhao, *Adv. Mater.*, 2022, **34**, 202106541.
12 S. Ji, Y. Chen, X. Wang, Z. Zhang, D. Wang and Y. Li, *Chem. Rev.*, 2020, **120**, 11900–11955.
13 Y. Chen, S. Ji, C. Chen, Q. Peng, D. Wang and Y. Li, *Joule*, 2018, **2**, 1242–1264.
14 L. Jiao, J. Li, L. L. Richard, Q. Sun, T. Stracensky, E. Liu, M. T. Sougrati, Z. Zhao, F. Yang, S. Zhong, H. Xu, S. Mukerjee, Y. Huang, D. A. Cullen, J. H. Park, M. Ferrandon, D. J. Myers, F. Jaouen and Q. Jia, *Nat. Mater.*, 2021, **20**, 1385–1391.
15 G. Wu, K. L. More, C. M. Johnston and P. Zelenay, *Science*, 2011, **332**, 443–447.
16 J. S. Bates, S. Biswas, S.-E. Suh, M. R. Johnson, B. Mondal, T. W. Root and S. S. Stahl, *J. Am. Chem. Soc.*, 2022, **144**, 922–927.
17 F. Hu, D. S. Yu, M. Ye, H. Wang, Y. A. Hao, L. Q. Wang, L. L. Li, X. P. Han and S. J. Peng, *Adv. Energy Mater.*, 2022, **12**, 2200067.
18 K. Shen, X. D. Chen, J. Y. Chen and Y. W. Li, *ACS Catal.*, 2016, **6**, 5887–5903.
19 J. Wu, Z. Meng, R. Zhang, T. Tian, R. Wang and H. Tang, *Energy Fuels*, 2022, **36**, 4006–4014.
20 J. N. Song, S. Y. Qiu, F. Hu, Y. H. Ding, S. L. Han, L. L. Li, H. Y. Chen, X. P. Han, C. H. Sun and S. J. Peng, *Adv. Funct. Mater.*, 2021, **31**, 2100618.
21 H. J. Huang, D. S. Yu, F. Hu, S. C. Huang, J. N. Song, H. Y. Chen, L. L. Li and S. J. Peng, *Angew. Chem., Int. Ed.*, 2022, **61**, e202116068.

22 F.-L. Meng, Z.-L. Wang, H.-X. Zhong, J. Wang, J.-M. Yan and X.-B. Zhang, *Adv. Mater.*, 2016, **28**, 7948–7955.

23 J. Xiao, Y. Xu, Y. Xia, J. Xi and S. Wang, *Nano Energy*, 2016, **24**, 121–129.

24 G. B. Chen, P. Liu, Z. Q. Liao, F. F. Sun, Y. H. He, H. X. Zhong, T. Zhang, E. Zschech, M. W. Chen, G. Wu, J. Zhang and X. L. Feng, *Adv. Mater.*, 2020, **32**, 1907399.

25 S. Li, W. Chen, H. Pan, Y. Cao, Z. Jiang, X. Tian, X. Hao, T. Maiyalagan and Z.-J. Jiang, *ACS Sustainable Chem. Eng.*, 2019, **7**, 8530–8541.

26 L. Jiao, R. Zhang, G. Wan, W. Yang, X. Wan, H. Zhou, J. Shui, S. H. Yu and H. L. Jiang, *Nat. Commun.*, 2020, **11**, 2831.

27 J. Wang and F. Ciucci, *Small*, 2017, **13**, 201604103.

28 J. B. Angus Pedersen, A. Li, R. Jervis, D. J. L. Brett, M. Magdalena Titirici and I. E. L. Stephens, *Adv. Energy Mater.*, 2022, **12**, 2102715.

29 K. H. Wu, Y. Liu, X. Tan, Y. Liu, Y. Lin, X. Huang, Y. Ding, B. J. Su, B. Zhang and J. M. Chen, *Chem Catal.*, 2022, **2**, 372–385.

30 Y. Hao, F. Hu, Y. Chen, Y. Wang, J. Xue, S. Yang and S. Peng, *Adv. Fiber Mater.*, 2022, **4**, 185–202.

31 C. Zhu, Q. Shi, B. Z. Xu, S. Fu, G. Wan, C. Yang, S. Yao, J. Song, H. Zhou, D. Du, S. P. Beckman, D. Su and Y. Lin, *Adv. Energy Mater.*, 2018, **8**, 1801956.

32 Z. Y. Du, P. Yu, L. Wang, C. G. Tian, X. Liu, G. Y. Zhang and H. G. Fu, *Sci. China Mater.*, 2020, **63**, 327–338.

33 X. Zhang, Z. Zhu, Y. Tan, K. Qin, F.-X. Ma and J. Zhang, *Chem. Commun.*, 2021, **57**, 2049–2052.

34 J. Wang, Z. Q. Huang, W. Liu, C. R. Chang, H. L. Tang, Z. J. Li, W. X. Chen, C. J. Jia, T. Yao, S. Q. Wei, Y. Wu and Y. D. Lie, *J. Am. Chem. Soc.*, 2017, **139**, 17281–17284.

35 C. Y. Su, H. Cheng, W. Li, Z. Q. Liu, N. Li, Z. F. Hou, F. Q. Bai, H. X. Zhang and T. Y. Ma, *Adv. Energy Mater.*, 2017, **7**, 201602420.

36 H. X. Xu, D. J. Cheng, D. P. Cao and X. C. Zeng, *Nat. Catal.*, 2018, **1**, 339–348.

37 P. Du, Y. Bao, C. Guo, L. Wu, J. Pan, C. Zhao, F.-X. Ma, J. Lu and Y. Y. Li, *Chem. Commun.*, 2020, **56**, 14467–14470.

38 X. Zhang, Z. Zhu, X. Liang, F.-X. Ma, J. Zhang, Y. Tan, Z. Pan, Y. Bo and C.-M. L. Wu, *Chem. Eng. J.*, 2021, **408**, 127270.

39 D. Peng, X. Xiao, F. Ma, H. Wang, J. Shen, F. Lyu, Y. Chen, J. Lu and Y. Li, *ACS Appl. Nano Mater.*, 2020, **3**, 5637–5644.

40 P. Du, F.-X. Ma, F. Lyu, K. He, Z. Li, J. Lu and Y. Y. Li, *Chem. Commun.*, 2019, **55**, 5789–5792.

41 L. Yang, X. F. Zeng, W. C. Wang and D. P. Cao, *Adv. Funct. Mater.*, 2018, **28**, 1704537.

42 G. Fu, X. Yan, Y. Chen, L. Xu, D. Sun, J.-M. Lee and Y. Tang, *Adv. Mater.*, 2018, **30**, 1704609.

43 F.-X. Ma, C.-Y. Xu, F. Lyu, B. Song, S.-C. Sun, Y. Y. Li, J. Lu and L. Zhen, *Adv. Sci.*, 2019, **6**, 201801490.

44 Y. F. Dong, M. L. Yu, Z. Y. Wang, Y. Liu, X. Z. Wang, Z. B. Zhao and J. S. Qiu, *Adv. Funct. Mater.*, 2016, **26**, 7590–7598.

45 P. Du, X. Xiao, F. Ma, H. Wang, J. Shen, F. Lyu, Y. Chen, J. Lu and Y. Li, *ACS Appl. Nano Mater.*, 2020, **3**, 5637–5644.

46 Y. Pan, Y. Chen, K. Wu, Z. Chen, S. Liu, X. Cao, W.-C. Cheong, T. Meng, J. Luo, L. Zheng, C. Liu, D. Wang, Q. Peng, J. Li and C. Chen, *Nat. Commun.*, 2019, **10**, 4290.

47 H. M. A. Sadezky, H. Grothe, R. Niessner and U. Poschl, *Carbon*, 2005, **43**, 1731–1742.

48 J. Zhang, Y. Sun, J. Zhu, Z. Kou, P. Hu, L. Liu, S. Li, S. Mu and Y. Huang, *Nano Energy*, 2018, **52**, 307–314.

49 X. Chen, D.-D. Ma, B. Chen, K. Zhang, R. Zou, X.-T. Wu and Q.-L. Zhu, *Appl. Catal., B*, 2020, **267**, 118720.

50 C. Shao, S. Zhuang, H. Zhang, Q. Jiang, X. Xu, J. Ye, B. Li and X. Wang, *Small*, 2021, **17**, e2006178.

51 F. X. Ma, G. Zhang, M. Wang, X. Liang, F. Lyu, X. Xiao, P. Wang, L. Zhen, J. Lu, L. Zheng, Y. Yang Li and C. Y. Xu, *J. Colloid Interface Sci.*, 2022, **620**, 67–76.

52 S. Yang, X. Feng, X. Wang and K. Muellen, *Angew. Chem., Int. Ed.*, 2011, **50**, 5339–5343.

53 J. Luo, K. Wang, X. Hua, W. Wang, J. Li, S. Zhang and S. Chen, *Small*, 2019, **15**, 201805325.

54 Y. Pan, S. Liu, K. Sun, X. Chen, B. Wang, K. Wu, X. Cao, W.-C. Cheong, R. Shen, A. Han, Z. Chen, L. Zheng, J. Luo, Y. Lin, Y. Liu, D. Wang, Q. Peng, Q. Zhang, C. Chen and Y. Li, *Angew. Chem., Int. Ed.*, 2018, **57**, 8614–8618.